Journal of Biomedical Optics

BiomedicalOptics.SPIEDigitalLibrary.org

Use of acoustic reflector to make a compact photoacoustic tomography system

Sandeep Kumar Kalva
Manojit Pramanik

SPIE.

Sandeep Kumar Kalva, Manojit Pramanik, "Use of acoustic reflector to make a compact photoacoustic tomography system," *J. Biomed. Opt.* **22**(2), 026009 (2017), doi: 10.1117/1.JBO.22.2.026009.

Use of acoustic reflector to make a compact photoacoustic tomography system

Sandeep Kumar Kalva and Manojit Pramanik*
Nanyang Technological University, School of Chemical and Biomedical Engineering, Singapore

Abstract. A typical photoacoustic tomography (PAT) system uses a Q-switched Nd:YAG laser for irradiating the sample and a single-element ultrasound transducer (UST) for acquiring the photoacoustic data. Conventionally, in PAT systems, the UST is held in a horizontal position and moved in a circular motion around the sample in full 2π radians. Horizontal positioning of the UST requires a large water tank to house, and load on the motor is also high. To overcome this limitation, we used the UST in the vertical plane instead of the horizontal plane. The photoacoustic (PA) waves generated from the sample are directed to the detector surface using an acoustic reflector placed at 45 deg to the transducer body. Hence, we can reduce the scanning radius, which, in turn, will reduce the size of the water tank and load on the motor, and the overall conventional PAT system size can be minimized. In this work, we demonstrate that with this system configuration, we acquire nearly similar images for phantom and *in vivo* data as that of the conventional PAT system using both flat and focused USTs. [DOI: 10.1117/1.JBO.22.2.026009]

Keywords: photoacoustic tomography; acoustic reflector; small animal imaging.

Paper 160716R received Oct. 17, 2016; accepted for publication Feb. 8, 2017; published online Feb. 24, 2017.

1 Introduction

Photoacoustic tomography (PAT) is an evolving biomedical imaging modality with high feasibility of translating from bench to bed side clinical usage.[1–6] It is a noninvasive imaging technique that provides high ultrasonic resolution and rich optical contrast photoacoustic (PA) images. PAT imaging has been successfully used for brain imaging,[7] molecular imaging,[8] tumor angiogenesis,[9] sentinel lymph node imaging,[10,11] breast cancer imaging,[12,13] measuring deoxyhemoglobin (HbR) and oxyhemoglobin (HbO_2) concentration,[14] monitoring temperature,[15] and so on.[16–18] In conventional PAT systems, a Q switched Nd:YAG pulsed laser beam illuminates the target object, such as biological tissue. The tissue chromophores—like melanin, red blood cells, water—absorb this incident light energy. This increases the local temperature, which results in thermoelastic expansion of the tissue, and pressure waves (also known as photoacoustic waves or PA waves) are generated. These PA waves are detected by ultrasound transducers (USTs) around the tissue and are used to reconstruct the cross-sectional images of the initial pressure rise, which is related to the optical absorption map inside the tissue. Various reconstruction algorithms can be used to obtain this initial pressure map.[19–25]

In a PAT scanner, various types of transducers, such as single-element UST,[19] linear arrays,[11,26] semicircular array,[27] and circular array transducers[28] can be used to acquire the PA signals from the target object. Using a single-element detector, data acquisition can be done in two ways: (a) a stop-and-go scan and (b) a continuous scan. Continuous scanning is much faster compared to stop-and-go scanning. As only one detector is used to rotate around the sample, the imaging speed with single-element transducer is slow (several minutes) compared to array transducers (few seconds to few milliseconds depending on the array configuration) in which multiple detectors are used. However, array transducers are very expensive and require multichannel parallel amplification and data acquisition systems, whereas the single-element USTs are cheap and require single amplifier and single channel data acquisition systems. Recently, single-element transducers were used for high-speed PAT imaging using pulsed laser diode (PLD) based PAT[29,30] and slip-ring based PAT[31] systems. However, the single-element transducers are inconvenient to use as they need a larger radius to scan around the sample and, hence, a larger water tanks.

For deep tissue imaging, the PA signal is collected by positioning the UST in orthogonal mode (perpendicular to the laser irradiation and facing toward the center in a circular scanning geometry). The sample and the UST are placed in a water bath for better acoustic coupling. Due to the length of the transducer body and part of the connecting cable [Fig. 1(a)], the UST needs more space to rotate around the sample. To house this type of UST and part of connecting cable, a large water tank is required, which, in turn, occupies a large space. Also, there is an increased load on the motor as the scanning radius of the UST is large. One way to reduce the scanning radius is to use a custom-made UST of shorter length that occupies less space. Typically, such custom made detectors increase the cost of the overall system and may not be easily available. To overcome such limitations, instead of positioning the UST in the horizontal direction, we propose positioning it in the vertical direction. The generated PA waves from the sample are directed toward the detector using an acoustic reflector. The surface of the acoustic reflector is made of stainless steel. This acoustic reflector is attached to the transducer body with the reflector surface at 45 deg to the detector surface [Fig. 1(a)]. Thus, this configuration brings down the water tank size significantly and reduces the scanning radius. Since the scanning radius is reduced, the load on the stepper motor can also be reduced. Hence, the overall PAT system

*Address all correspondence to: Manojit Pramanik, E-mail: manojit@ntu.edu.sg

1083-3668/2017/$25.00 © 2017 SPIE

size can be reduced, which will be very helpful in designing a more compact and portable PAT system.

In this work, it has been shown that nearly similar images are obtained using an ultrasound transducer with reflector (USTR) compared to that of a conventional UST. Three different types of phantom imaging were used for demonstration: (a) point sources (pencil leads of 0.5 mm diameter), (b) horse hair (150-μm thickness) phantom arranged in a triangular shape, and (c) "N" shaped low density polyethylene (LDPE) tubes of 0.38 mm diameter filled with rat blood mimicking the blood vessels embedded inside chicken breast tissue and *in vivo* rat brain imaging. A simple delay-and-sum reconstruction algorithm has been used to reconstruct the PA images.[19,20]

2 Materials and Methods

2.1 *Photoacoustic Tomography Imaging System*

The PAT imaging system used is shown in Fig. 1(b). Here, a Q-switched Nd:YAG laser (Continuum, Surelite Ex) delivers laser pulses of 10 Hz at 532-nm wavelength (5-ns pulse width). Three right-angle uncoated prisms (PS911, Thorlabs) (not shown in the schematic) and one uncoated planoconcave lens L1 (LC1715, Thorlabs) were used to deliver the laser pulses from the Nd:YAG laser to the sample. The laser energy density was maintained at ~9 mJ/cm^2 on the sample surface, which is much lower than the ANSI safety limit[32] of 20 mJ/cm^2 at 400 to 700 nm. For point source and hair phantoms, a 532-nm wavelength laser was used. In biological tissue, the light penetration is greater in the near-infrared (NIR) wavelength region, so an optical parametric oscillator (OPO) laser (Continuum, Surelite) pumped by the Q-switched (532 nm) laser was used as the light excitation source for "N" shaped blood vessel mimicking phantom and *in vivo* rat brain imaging. The OPO laser was set to deliver laser pulses of 680-nm wavelength to the sample. Three right-angle coated prisms P1, P2, and P3 (PS908L-B, Thorlabs) and one uncoated planoconcave lens L1 [LC1715, Thorlabs; Fig. 1(b)] were used to deliver the laser pulses from OPO to the sample. The laser energy density was maintained at ~6 mJ/cm^2 on the sample surface. A flat UST (Olympus NDT, V306-SU), a flat USTR by attaching an acoustic reflector (F102, Olympus NDT) with the flat UST, a focused UST (Olympus NDT, V306-SU-NK, CF = 1.90 in.), and a focused USTR by attaching the same acoustic reflector to the focused UST were used to acquire the PA signal. The UST had a 2.25-MHz central frequency with ~70% nominal bandwidth and 13-mm diameter detector surface area. Figure 1(a) shows the flat UST, the acoustic reflector, and the acoustic reflector attached with the flat UST. Each UST acquires the PA data by moving around the sample in full 2π radians in circular geometry. In all the experiments, the PA signals were collected continuously for 480 s with UST at a rotational speed of 0.75 deg/s. The acquired PA signals were regrouped into 800 A-lines. The acquired PA signals were first amplified and filtered using a pulse amplifier (Olympus-NDT, 5072PR) and then recorded using a data acquisition (DAQ) card (GaGe, compuscope 4227) inside a desktop (Intel xeon 3.7 GHz 64-bit processor, 16 GB RAM, running Windows 10 operating system). All PA data were acquired with a 25-MHz sampling rate. The data acquisition was synchronized with the laser illumination with a TTL sync signal from the laser.

2.2 *Phantom Experiments*

Figures 1(c)–1(e) show the phantoms used for the experiments. The first phantom was a point source object made using five pencil leads of 0.5 mm diameter held using a pipette and adhered to an acrylic slab [Fig. 1(c)]. One pencil lead was placed at the scanning center, and four other pencil leads were placed at a distance of ~1 cm from the scanning center. Figure 1(d) shows the second phantom made of horse hair of 150 μm thickness in

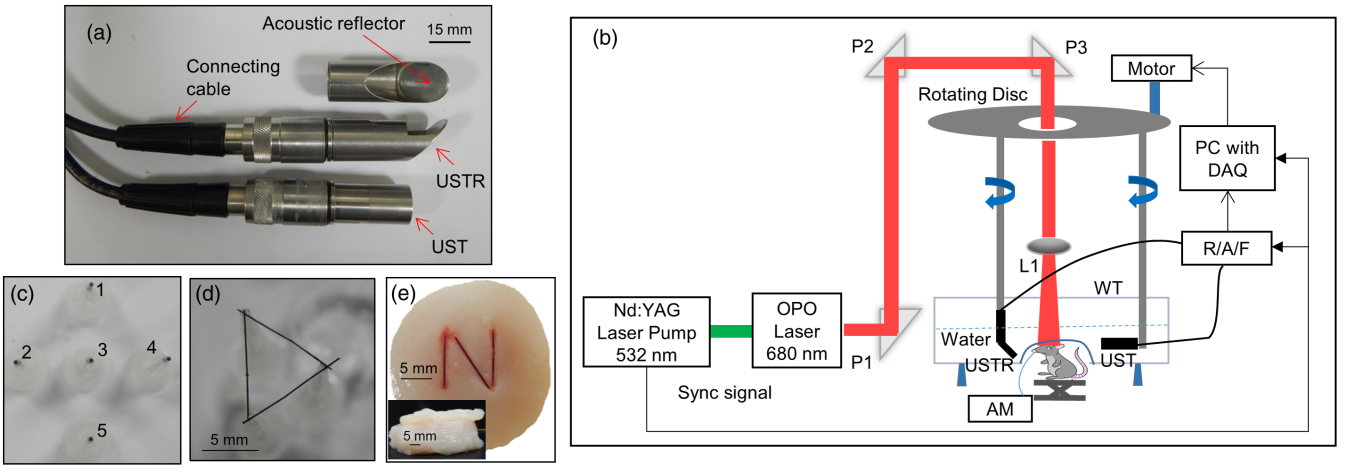

Fig. 1 (a) Images of conventional ultrasound transducer (UST), UST with acoustic reflector (USTR), and acoustic reflector. (b) Schematic diagram of the PAT imaging system used in this work. R/A/F: receiver, amplifier, and filter for PA signal; DAQ: data acquisition card; P1, P2, and P3 are coated prisms; L1: planoconcave lens, rotating disc (connected to UST and controlled by a stepper motor); AM: anaesthesia machine, WT: water tank. The UST and sample are immersed in water bath for better acoustic coupling. (c) Point source phantom made using 0.5 mm diameter pencil leads (one at the center and 4 others placed at ~1 cm from the center). (d) Triangular shaped horse hair phantom (150 μm thickness). (e) "N" shaped blood vessel phantom made using low density polyethylene (LDPE) tubes of 0.38 mm diameter embedded inside chicken breast tissue layer. On top of this layer, a 5-mm thick chicken breast tissue was placed [inset in Fig. 1(e)].

triangular shape glued to the tips of pipettes and adhered to an acrylic slab. Each side of the triangle is ~1 cm. The third phantom was the blood vessel phantom made by LDPE tubes of 0.38 mm diameter filled with rat blood. These tubes were embedded inside a layer of chicken breast tissue in the shape of "N" [Fig. 1(e)]. Another chicken breast tissue layer of 5 mm thickness was placed on top [Fig. 1(e) inset]. All these phantoms were placed inside a water bath for better acoustic coupling.

2.3 *In Vivo Experiments*

In vivo animal experiments were conducted using healthy female rats weighing ~120 g. The rats were procured from InVivos Pte. Ltd., Singapore. Animal experiments were performed according to the approved guidelines and regulations by the institutional Animal Care and Use committee of Nanyang Technological University, Singapore (Animal Protocol Number ARF-SBS/NIE-A0263). The animals were anesthetized using a cocktail of Ketamine (120 mg/kg) and Xylazine (16 mg/kg) injected intraperitoneally (dosage of 0.2 ml/100 g). Before the animals were placed in the PAT scanner, the hair on the head was trimmed and then epilated using hair removal cream. A breathing mask covering the mouth and nose of the animal was used to deliver an anesthesia mixture of isoflurane and O_2 during PAT imaging. The animal was placed in a sitting position on its abdomen using a custom-made animal holder. Surgical tapes were used to hold the animal in its position. The animal along with the animal holder was mounted on a translational stage during the experiment. The translational stage was used to adjust the height of the animal to adjust the scan plane of the brain. After the data acquisition, animals were euthanized by intraperitoneal injection of Valabarb (sodium pentobarbitone 300 mg/ml).

2.4 *Comparison of Reconstructed Images*

To study the quality of the images obtained using an acoustic reflector, a signal-to-noise ratio (SNR) was calculated for both flat and focused transducers and compared with SNR levels of the images obtained using unfocused and focused transducers without an acoustic reflector. The SNR was calculated from the reconstructed PAT images as the ratio of PA amplitude to the standard deviation of the background noise, i.e., SNR (in dB) $=20\log(V/n)$, where V is the PA amplitude on the object and n is the standard deviation of the background noise. For point source phantom, PA amplitude was calculated for the point 3 in Fig. 1(c), and, in all the other cases, PA amplitude was calculated as the average of the PA amplitude of the whole target object. The noise was taken from the background where there was no object located.

3 Results and Discussions

3.1 *Phantom Experiments*

Figure 2 shows the reconstructed PA images of point objects (pencil leads located one at center and four at ~1 cm distance from the center). Figure 2(a) shows the reconstructed PAT images

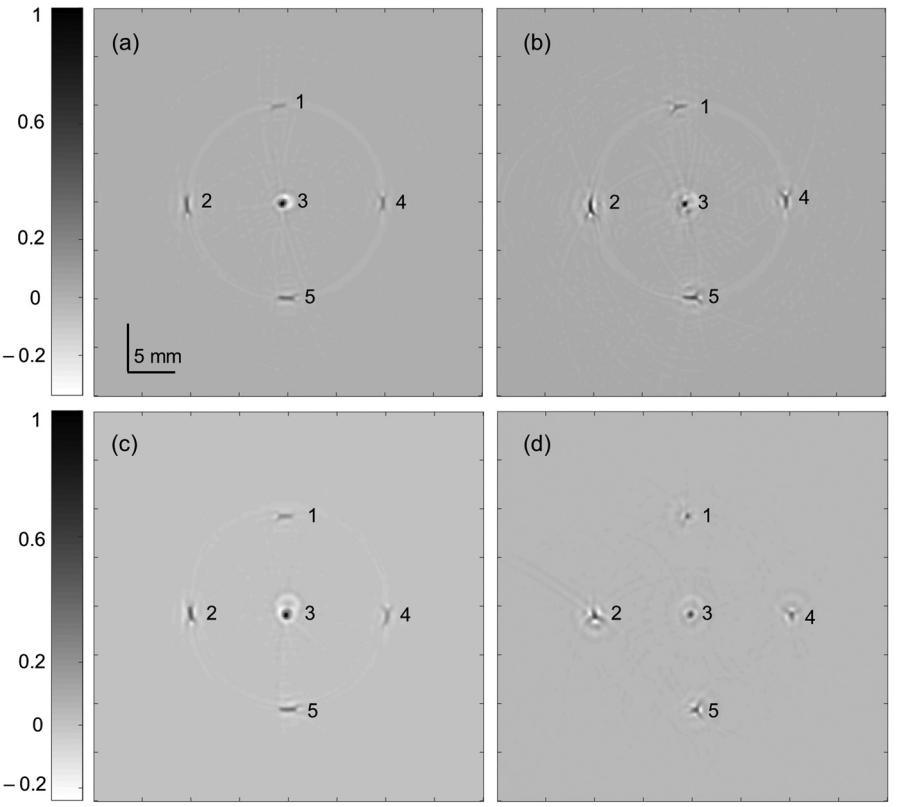

Fig. 2 Cross-sectional reconstructed PAT images of the point source phantom. (a) Reconstructed PAT image obtained using flat UST, (b) reconstructed PAT image obtained using flat USTR, (c) reconstructed PAT image obtained using focused UST, (d) reconstructed PAT image obtained using focused USTR. Corresponding color bars are shown for images of flat and focused transducers. Scale bar is shown in (a) for all the images.

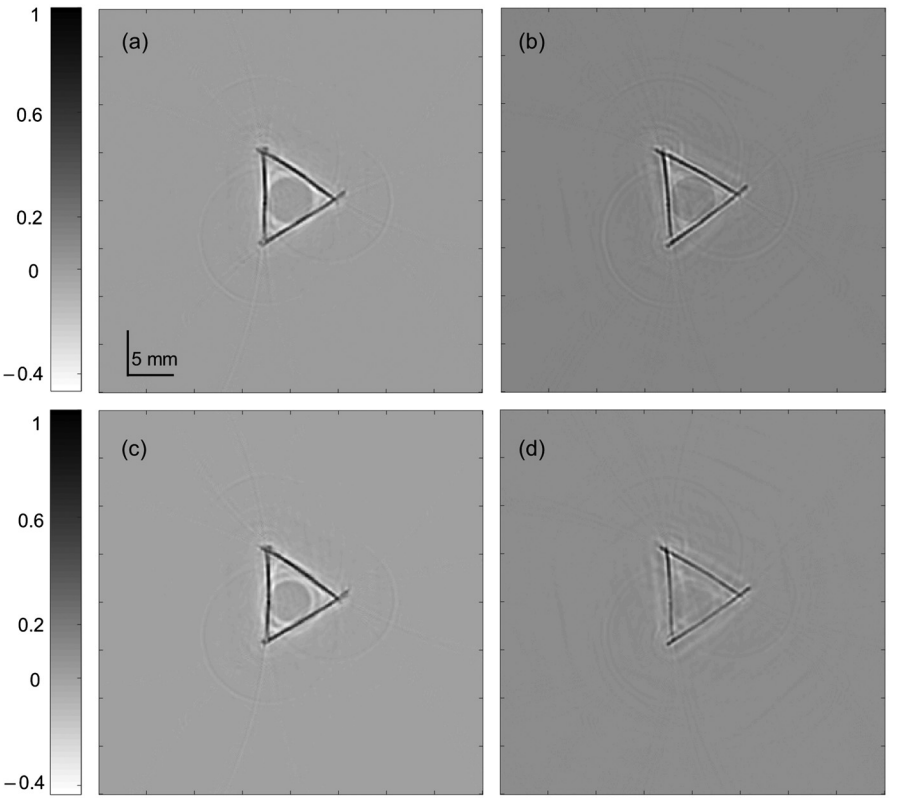

Fig. 3 Cross-sectional reconstructed PAT images of triangular shaped hair phantom. (a) Reconstructed PAT image for flat UST, (b) reconstructed PAT image for flat USTR, (c, d) reconstructed PAT images for focused UST and focused USTR, respectively. Corresponding color bars are shown for flat and focused transducers. Scale bar is shown in (a) for all the images.

of the point targets using a flat UST, and Fig. 2(b) shows the reconstructed PA images using a flat USTR. Figures 2(c) and 2(d) show the reconstructed PA images obtained using a cylindrically focused UST and a cylindrically focused USTR, respectively. To study the quality of the images, the SNR was calculated (for point target 3). The SNR value with the flat UST was 54.9 dB and with the flat USTR was 50.56 dB. There was an ∼8% reduction in the SNR with the flat USTR. Corresponding SNR values for the focused UST and the focused USTR were calculated to be 48.18 and 47.76 dB, respectively. There was an ∼0.8% degradation in the SNR with the focused USTR.

Next, a study was conducted using a horse hair triangular phantom. The hair was 150 μm thick. Each side was ∼1 cm in length. Figure 3(a) shows the reconstructed PAT image of the hair phantom using a flat UST, and Fig. 3(b) shows the reconstructed PA image using a flat USTR. Corresponding SNR values for these images were calculated to be 47.44 and 47.56 dB, respectively. SNR levels were maintained for flat USTR as well as those of flat UST. Figures 3(c) and 3(d) show the reconstructed PA images using focused transducers without and with an acoustic reflector, respectively. For these images, SNR values were computed to be 48.8 and 45.85 dB, respectively. The SNR was ∼6% lower using a cylindrically focused transducer with an acoustic reflector compared to its counterpart.

Next, an "N" shaped blood vessel phantom (LDPE tubes of 0.38 mm diameter) of ∼1 cm × 1 cm dimensions embedded inside a chicken breast tissue layer was studied. A layer of 5-mm thick chicken breast tissue was placed on top of this layer. The reconstructed PAT images for unfocused UST and unfocused USTR are shown in Figs. 4(a) and 4(b), respectively. The corresponding SNR levels for these images were computed to be 24.61 and 24.32 dB, resepctively. Figures 4(c) and 4(d) show cross-sectional reconstructed PA images obtained through a cylindrically focused transducer without and with acoustic reflector, respectively. The SNR values were calculated to be 30.56 and 31.01 dB, respectively. The SNR was ∼1.5% higher using a focused USTR than a focused UST.

3.2 *In Vivo Experiments*

Next, a study was conducted on small animals to demonstrate the feasibility of using an acoustic reflector augmented to a conventional UST to obtain similar quality images to that of a conventional UST. As described earlier, anesthetized healthy female rats were used for this study. Figure 5 shows the cross-sectional reconstructed PAT images of the animal brain. The images obtained for flat UST without and with acoustic reflector are shown in Figs. 5(a) and 5(b), respectively. Figure 5(c) shows the cross-sectional reconstructed PA image of the focused UST, and Fig. 5(d) shows the cross-sectional reconstructed PA image of the focused USTR. In all four images, superior sagittal sinus (SS) and transverse sinuses (TS) were clearly visible (yellow arrows). Figure 5(e) shows the image of the animal head before taking PAT images, and Fig. 5(f) shows the image of the animal brain after cutting open the top layer of skin on the head after the image acquisition was completed. To study the quality of the images, the SNR was calculated. The SNR was 22.76 dB (flat UST) and 18.66 dB (flat USTR). There was an ∼18% reduction in the SNR levels with the usage of an acoustic reflector. The

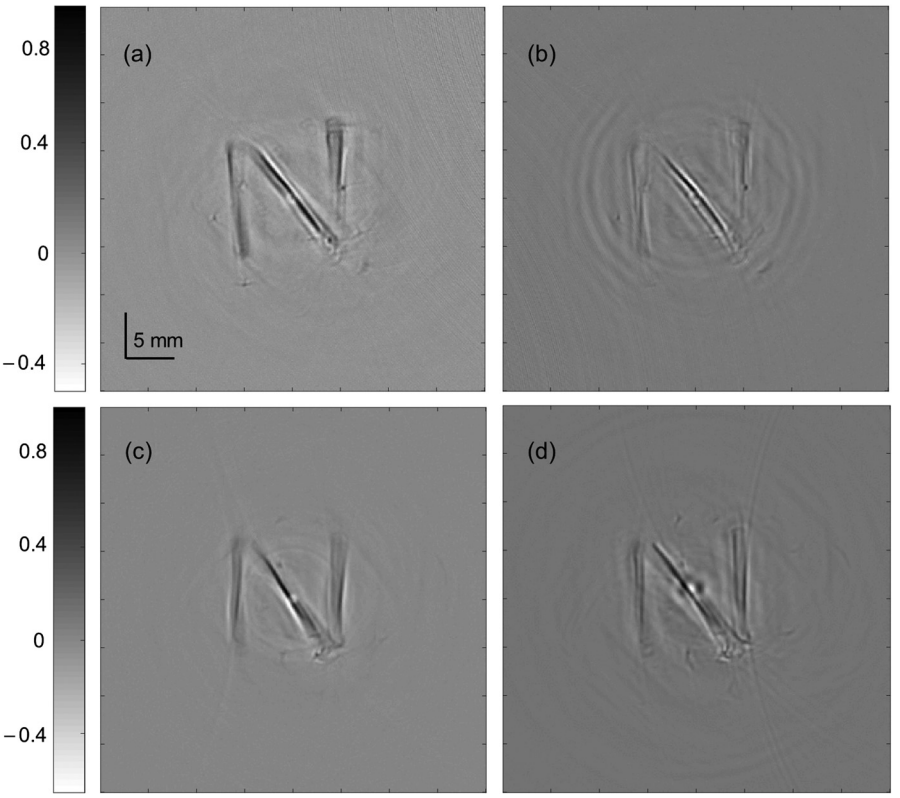

Fig. 4 Cross-sectional reconstructed PAT images of "N" shaped blood vessel phantom embedded inside chicken breast tissue. (a) Reconstructed PAT image for flat UST, (b) reconstructed PAT image obtained using flat USTR, (c) cross-sectional reconstructed PAT image for focused UST, (d) cross-sectional reconstructed PAT image obtained using focused USTR. Corresponding color bars are shown for the images of flat and cylindrically focused transducers. Scale bar is shown in (a) for all the images.

SNR for the images obtained with the focused UST was 26.61 dB and that for the focused USTR was 31.63 dB. There was a ∼19% enhancement in the SNR levels using the focused transducer with an acoustic reflector compared to that of the images from the focused transducer without an acoustic reflector.

The ultrasound waves generated from the sample fall at 45 deg to the water and acoustic reflector (stainless steel) interface. At this incidence angle, due to the total internal reflection phenomenon, the ultrasound waves are entirely reflected back into the water medium. These reflected waves are detected by the UST. As discussed above, the SNR was maintained in many cases, but there was an $\sim(1\text{ to }19)\%$ enhancement or degradation in the SNR levels for a few cases. This was due to the small difference (∼2 to 3 mm) in the distance at which the UST and USTR were placed from the scanning center. The amplitude of the ultrasound signal detected by the UST is inversely proportional to the square of the distance from the source (target object) to the detector surface, so the small difference in the distances results in SNR variations. If the scanning radii were kept exactly the same for the UST and USTR, then SNR levels in these cases would also have been similar. Visually, the quality of the PAT images obtained using an acoustic reflector augmented to the conventional USTs was nearly similar to that of the PAT images obtained using conventional transducers of both flat and focused UST.

For better understanding of the quality of the PAT images using an acoustic reflector, the resolution of the PAT system was compared for all four transducers. The resolution was calculated using full-width at half-maximum from the point spread function of the hair phantom images. For flat UST and flat USTR, the resolution was 301 and 281 μm, respectively. For focused UST and focused USTR, it was computed to be 294 and 269 μm, respectively. This resolution matches well with the theoretically expected resolution of 250 μm for a 2.25 MHz UST, so the use of acoustic reflector did not affect the spatial resolution of the PAT system. The frequency response of the transducers with and without the reflector was also compared. As expected, we did not see any degradation of the transducer bandwidth with or without the reflector. The frequency response for all four transducers was calculated by taking Fourier transforms of the Aline PA signal (averaged six times) from the hair phantom. The bandwidth was calculated from the frequency response. The bandwidth for flat UST, flat USTR, focused UST, and focused USTR was found to be 2.29, 2.24, 2.46, and 2.44 MHz, respectively.

Hence, by using the acoustic reflector augmented to the conventional UST surface at 45 deg, we can use the transducer in the vertical plane instead of the horizontal plane. Therefore, the transducer rotates in a smaller circle around the sample. This vertical configuration will lead to a size reduction of the water tank used for housing the transducer as well as the target object (the length and width of the tank will be reduced by ∼11.5 cm: this includes the length of the UST and partial length of the connecting cable). This reduces the volume of the PAT system. Also, the load on the motor that rotates the UST decreases as the torque required to rotate the UST decreases. Hence, the overall PAT system size can be minimized. Together

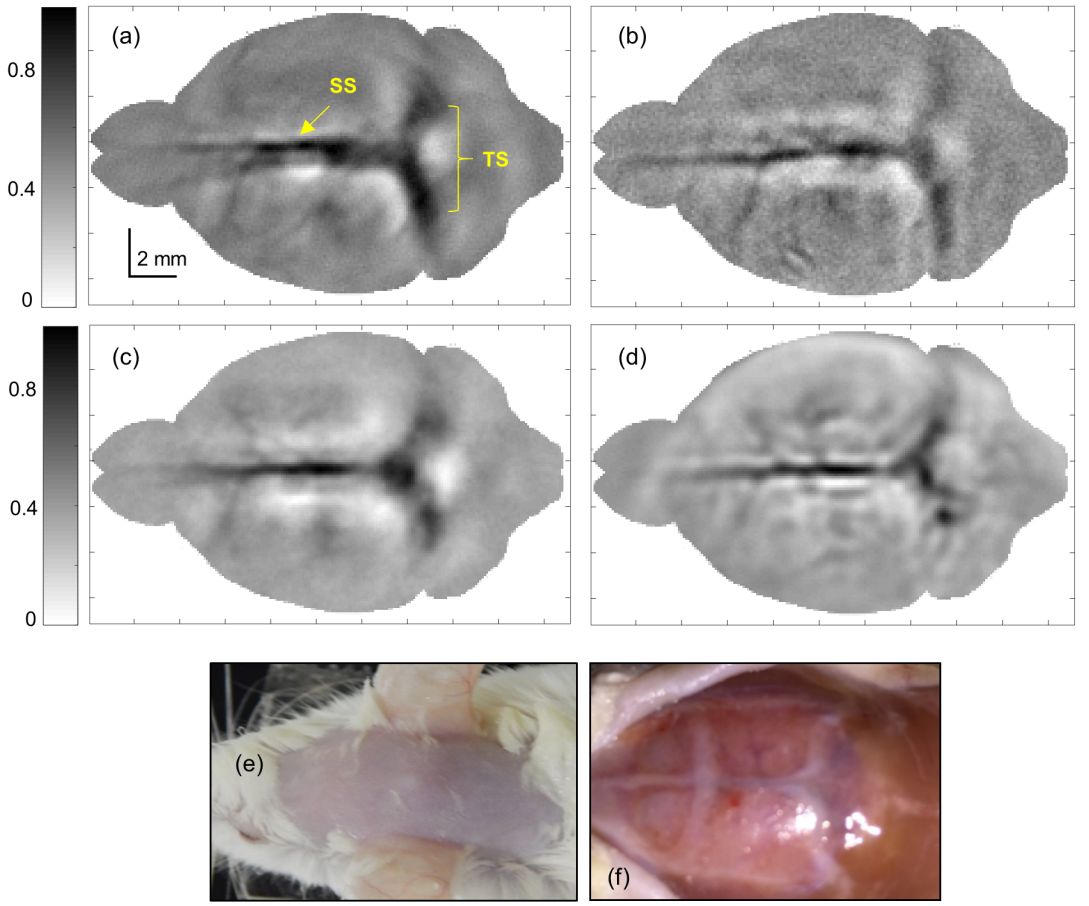

Fig. 5 Reconstructed cross-sectional PAT images of rat brain. (a) Reconstructed PAT image for flat UST, (b) reconstructed cross-sectional PAT image for flat USTR, (c) cross-sectional reconstructed PAT image obtained using focused UST, (d) reconstructed cross-sectional PAT images obtained using focused USTR. SS: superior sagittal sinus, TS: transverse sinus. Yellow arrows point to the SS, TS. Corresponding color bars are shown for unfocused and cylindrically focused transducers. Scale bar is shown in (a) for all the images. (e) Rat brain after trimming and removal of hair on the head region before PAT imaging. (f) Rat brain after cutting open the top skin layer of the head region after the PAT imaging is completed.

with a PLD-based PAT system,[30] this configuration of UST will make the entire PAT system quite compact and hopefully translation to clinical applications will be easier. As the use of the acoustic reflector did not affect the SNR levels or the spatial resolution (as well as the bandwidth of the ultrasound detectors) of the PAT system, this acoustic reflector can be used with any PAT system in which single-element USTs with circular scanning geometry are used. This will reduce the scanning radius and will make the PAT imaging system more compact in size. The USTR-based PAT system can find applications in small animal brain imaging, breast cancer imaging, etc.

4 Conclusion

By attaching an acoustic reflector made of stainless steel to a conventional single-element UST, we obtained nearly similar quality PAT images as that of the conventional single-element UST for both flat and cylindrically focused UST. Phantoms as well as *in vivo* results confirm that this vertical configuration of the UST will be quite useful for making even more compact PAT systems. This is the first report on using the UST in the vertical position for PAT, and this will also be useful for similar scanner using thermoacoustic tomography.

Disclosures

Authors have no relevant financial interests in the manuscript and no other potential conflicts of interest to disclose.

Acknowledgments

The authors would like to thank Ms. Vijitha Periyasamy for assisting in animals experiments. The authors would also like to acknowledge financial support from the Tier 1 grant funded by the Ministry of Education in Singapore (RG31/14: M4011276, RG41/14: M4011285) and the Singapore National Research Foundation administered by the Singapore Ministry of Health's National Medical Research Council (NMRC/OFIRG/0005/2016: M4062012).

References

1. L. V. Wang and J. Yao, "A practical guide to photoacoustic tomography in the life sciences," *Nat. Methods* **13**(8), 627–638 (2016).
2. Y. Zhou, J. Yao, and L. V. Wang, "Tutorial on photoacoustic tomography," *J. Biomed. Opt.* **21**(6), 061007 (2016).
3. L. V. Wang and S. Hu, "Photoacoustic tomography: in vivo imaging from organelles to organs," *Science* **335**(6075), 1458–1462 (2012).

4. C. Li and L. V. Wang, "Photoacoustic tomography and sensing in biomedicine," *Phys. Med. Biol.* **54**(19), R59–R97 (2009).
5. L. V. Wang, "Multiscale photoacoustic microscopy and computed tomography," *Nat. Photonics* **3**(9), 503–509 (2009).
6. L. V. Wang, "Prospects of photoacoustic tomography," *Med. Phys.* **35**(12), 5758–5767 (2008).
7. X. Yang and L. V. Wang, "Monkey brain cortex imaging by photoacoustic tomography," *J. Biomed. Opt.* **13**(4), 044009 (2008).
8. J. Yao, J. Xia, and L. V. Wang, "Multiscale functional and molecular photoacoustic tomography," *Ultrason. Imaging* **38**(1), 44–62 (2016).
9. G. Ku et al., "Imaging of tumor angiogenesis in rat brains in vivo by photoacoustic tomography," *Appl. Opt.* **44**(5), 770–775 (2005).
10. A. Garcia-Uribe et al., "Dual-modality photoacoustic and ultrasound imaging system for noninvasive sentinel lymph node detection in patients with breast cancer," *Sci. Rep.* **5**, 15748 (2015).
11. T. N. Erpelding et al., "Sentinel lymph nodes in the rat: noninvasive photoacoustic and US imaging with a clinical US system," *Radiology* **256**(1), 102–110 (2010).
12. X. Wang et al., "Computational feasibility study of contrast-enhanced thermoacoustic imaging for breast cancer detection using realistic numerical breast phantoms," *IEEE Trans. Microwave Theory Tech.* **63**(5), 1489–1501 (2015).
13. M. Pramanik et al., "Design and evaluation of a novel breast cancer detection system combining both thermoacoustic (TA) and photoacoustic (PA) tomography," *Med. Phys.* **35**(6), 2218–2223 (2008).
14. E. W. Stein, K. Maslov, and L. V. Wang, "Noninvasive, in vivo imaging of blood-oxygenation dynamics within the mouse brain using photoacoustic microscopy," *J. Biomed. Opt.* **14**(2), 020502 (2009).
15. M. Pramanik and L. V. Wang, "Thermoacoustic and photoacoustic sensing of temperature," *J. Biomed. Opt.* **14**(5), 054024 (2009).
16. K. Sivasubramanian and M. Pramanik, "High frame rate photoacoustic imaging at 7000 frames per second using clinical ultrasound system," *Biomed. Opt. Express* **7**(2), 312–323 (2016).
17. K. Daoudi et al., "Handheld probe integrating laser diode and ultrasound transducer array for ultrasound/photoacoustic dual modality imaging," *Opt. Express* **22**(21), 26365–26374 (2014).
18. X. Cai et al., "Photoacoustic tomography of foreign bodies in soft biological tissue," *J. Biomed. Opt.* **16**(4), 046017 (2011).
19. S. K. Kalva and M. Pramanik, "Experimental validation of tangential resolution improvement in photoacoustic tomography using a modified delay-and-sum reconstruction algorithm," *J. Biomed. Opt.* **21**(8), 086011 (2016).
20. M. Pramanik, "Improving tangential resolution with a modified delay-and-sum reconstruction algorithm in photoacoustic and thermoacoustic tomography," *J. Opt. Soc. Am. A* **31**(3), 621–627 (2014).
21. M. Pramanik, G. Ku, and L. V. Wang, "Tangential resolution improvement in thermoacoustic and photoacoustic tomography using a negative acoustic lens," *J. Biomed. Opt.* **14**(2), 024028 (2009).
22. M. Xu and L. V. Wang, "Universal back-projection algorithm for photoacoustic computed tomography," *Phys. Rev. E* **71**(1), 016706 (2005).
23. Y. Xu, M. H. Xu, and L. V. Wang, "Exact frequency-domain reconstruction for thermoacoustic tomography - II: cylindrical geometry," *IEEE Trans. Med. Imaging* **21**(7), 829–833 (2002).
24. Y. Xu, D. Z. Feng, and L. V. Wang, "Exact frequency-domain reconstruction for thermoacoustic tomography - I: planar geometry," *IEEE Trans. Med. Imaging* **21**(7), 823–828 (2002).
25. M. Xu and L. V. Wang, "Pulsed-microwave-induced thermoacoustic tomography: filtered backprojection in a circular measurement configuration," *Med. Phys.* **29**(8), 1661–1669 (2002).
26. X. Wang et al., "Photoacoustic imaging with a commercial ultrasound system and a custom probe," *Ultrasound Med. Biol.* **37**(3), 484–492 (2011).
27. A. Buehler et al., "Three-dimensional optoacoustic tomography at video rate," *Opt. Express* **20**(20), 22712–22719 (2012).
28. C. Li et al., "Real-time photoacoustic tomography of cortical hemodynamics in small animals," *J. Biomed. Opt.* **15**(1), 010509 (2010).
29. P. K. Upputuri and M. Pramanik, "High-speed pre-clinical brain imaging using pulsed laser diode based photoacoustic tomography (PLD-PAT) system," *Proc. SPIE* **9708**, 97084R (2016).
30. P. K. Upputuri and M. Pramanik, "Performance characterization of low-cost, high-speed, portable pulsed laser diode photoacoustic tomography (PLD-PAT) system," *Biomed. Opt. Express* **6**(10), 4118–4129 (2015).
31. Z. Deng, W. Li, and C. Li, "Slip-ring-based multi-transducer photoacoustic tomography system," *Opt. Lett.* **41**(12), 2859–2862 (2016).
32. *American National Standard for Safe Use of Lasers ANSI Z136.1-2000*, Laser Institute of America, New York (2000).

Sandeep Kumar Kalva received his master's degree in biomedical engineering from the Indian Institute of Technology (IIT), Hyderabad, India, in 2015. He is currently a PhD student in the School of Chemical and Biomedical Engineering, Nanyang Technological University, Singapore. His research area is on functional photoacoustic imaging for various clinical applications.

Manojit Pramanik received his PhD in biomedical engineering from Washington University in St. Louis, Missouri, USA. Currently, he is an assistant professor of the School of Chemical and Biomedical Engineering, Nanyang Technological University, Singapore. His research interests include the development of photoacoustic/thermoacoustic imaging systems, image reconstruction methods, clinical application areas such as breast cancer imaging, molecular imaging, contrast agent development, and Monte Carlo simulation of light propagation in biological tissue.